MITSUBISHI ELECTRIC RESEARCH LABORATORIES
https://www.merl.com

High-Fidelity Simulation of Horizon-Based Optical Navigation with Open-Source Software

Shimane, Yuri; Miraldo, Pedro; Berntorp, Karl; Greiff, Marcus; Elango, Purnanand; Weiss, Avishai

TR2023-128 October 03, 2023

Abstract

In this work, a high-fidelity simulation environment for autonomous cislunar spacecraft navigation based on horizon-based optical navigation (OpNav) is developed. Spacecraft autonomy is becoming a critical need, both from a mission safety standpoint in case of communication failure with Earth, as well as a scalability standpoint as the number of deployed spacecraft increases dramatically in the coming years. Autonomy is of particular importance in deep space, where communication (and thus, navigation) relies on NASA's Deep Space Network (DSN), which will need to be rationed, or where links to DSN can fail (see, for example, the recent CAPSTONE mission). As spacecraft activity builds on the near rectilinear halo orbit (NRHO) that the Lunar Gateway will fly, autonomous navigation and station-keeping control methods that do not rely on DSN are required. This work details how a high-fidelity rendering-based simulation environment for horizon-based OpNav may be realized. While the environment is useful for any spacecraft transiting in the vicinity of the Moon, special considerations arising from conducting OpNav on an NRHO are highlighted. The proposed environment is tested by processing rendered images of the Moon along an NRHO using a state-of-the-art horizon-based OpNav technique, and insights on the accuracy of the obtainable position measurements are provided

International Astronautical Congress (IAC) 2023

Mitsubishi Electric Research Laboratories, Inc.
201 Broadway, Cambridge, Massachusetts 02139

IAC–23–C1.5.9

High-Fidelity Simulation of Horizon-Based Optical Navigation with Open-Source Software

Yuri Shimane[1], **Pedro Miraldo**[3], **Karl Berntorp**[3], **Marcus Greiff**[3], **Purnanand Elango**[2], **and Avishai Weiss**[3*]
[1]Georgia Institute of Technology, USA, yuri.shimane@gatech.edu
[2]University of Washington, USA, pelango@uw.edu
[3]Mitsubishi Electric Research Laboratories, USA, {miraldo,berntorp,greiff,weiss}@merl.com

Abstract

In this work, a high-fidelity simulation environment for autonomous cislunar spacecraft navigation based on horizon-based optical navigation (OpNav) is developed. Spacecraft autonomy is becoming a critical need, both from a mission safety standpoint in case of communication failure with Earth, as well as a scalability standpoint as the number of deployed spacecraft increases dramatically in the coming years. Autonomy is of particular importance in deep space, where communication (and thus, navigation) relies on NASA's Deep Space Network (DSN), which will need to be rationed, or where links to DSN can fail (see, for example, the recent CAPSTONE mission). As spacecraft activity builds on the near rectilinear halo orbit (NRHO) that the Lunar Gateway will fly, autonomous navigation and station-keeping control methods that do not rely on DSN are required. This work details how a high-fidelity rendering-based simulation environment for horizon-based OpNav may be realized. While the environment is useful for any spacecraft transiting in the vicinity of the Moon, special considerations arising from conducting OpNav on an NRHO are highlighted. The proposed environment is tested by processing rendered images of the Moon along an NRHO using a state-of-the-art horizon-based OpNav technique, and insights on the accuracy of the obtainable position measurements are provided. Realistic image-based position measurements are incorporated into an extended Kalman filter to simulate OpNav-only autonomous navigation.

Keywords: Optical navigation, NRHO, Autonomy

1. **Introduction**

The Moon has seen a resurgence of activity, with nation states and private enterprise sending, or planning to send, orbiters and landers, and deploying human outposts, e.g. the Lunar Orbital Platform-Gateway (LOP-G) [1, 2], as part of a renewed interest in exploring and, eventually, settling the Moon. This increased activity will stress the capacity of Deep Space Network (DSN)-class ground-based infrastructure that is used to provide communication and navigation to cislunar spacecraft, motivating the search for alternative solutions. Furthermore, as recently highlighted by the CAPSTONE mission [3], links to DSN may fail [4], jeopardizing mission safety. While the CAPSTONE spacecraft eventually regained communication ability [5], such events demonstrate the need for independent autonomous navigation solutions. Towards this end, the Lunar GNSS Receiver Experiment (LuGRE) will attempt to use GPS and Galileo signals in the lunar environment and on the lunar surface [6], and CAPSTONE is testing a new peer-to-peer autonomous navigation system that measures range and range-rate relative to NASA's Lunar Reconnaissance Orbiter (LRO) [3]. Looking further into the upcoming decades, the LunaNet [7] concept from NASA and ESA aims to provide a framework for an all-encompassing communication network that may also provide navigational service [8].

An alternative navigation approach is to autonomously process space-captured optical imagery. The history of optical navigation (OpNav) with humans in the loop dates back to the early days of spaceflight in the mid 20th century, when Apollo astronauts used nautical techniques, much like traditional mariners, to take sightings with a sextant [9, 10]. Space-based optical navigation has come a long way, with terrain-relative [11, 12] and proxim-

[1]Yuri interned at Mitsubishi Electric Research Laboratories during the development of this work.

[*]Corresponding Author.

ity operation applications [13] seeing increased usage, and the recent success of the DART Mission, which used the DRACO (Didymos Reconnaissance and Asteroid Camera for OpNav) telescope to image, navigate to, and collide with the asteroid Dimorphos [14]. Of interest in this work, horizon-based OpNav technology has recently matured, and was demonstrated by the Orion Multi-Purpose Crew Vehicle on the Artemis 1 mission [15,16]. Horizon-based OpNav uses the horizon, or *lit limb*, of a celestial body to provide information about the relative position of the observer with respect to the observed celestial body [17]. Combining optical observations of a celestial body with independent attitude information readily available, e.g. from a star tracker, yields inertial position measurements that may be used in a navigation filter to provide full spacecraft state estimation.

Many of the characteristics of optical-based measurements can only be well-understood through realistic imagery, such as the impact of terrain features, and the diminishing observability as a function of range from the observed celestial body in the camera boresight, amongst other effects. However, the difficulty in procuring a robust set of lunar images from verified true positions motivates the generation of synthetic imagery. To date, several works have explored the use of computer generated imagery to simulate OpNav. NASA's EDGE software [18] was used to generate synthetic imagery of the Moon as part of the validation of the Orion optical navigation system [19]. Vizard, which is part of the Basilisk software [20], is a Unity-based astrodynamics visualization library, that has been used for horizon-based OpNav in Mars [21] and near rectilinear halo orbit (NRHO) [22]. POV-Ray [23] is a ray-tracing program that has been used by multiple authors, including for Moon-relative horizon-based OpNav [24, 25], as well as terrain-relative applications [26]. Blender [27] is an open-source rendering engine with an active development community, and has previously been used for OpNav application in horizon-relative OpNav [28], proximity operations [29], small-body-relative motion [30], as well as for terrain-relative applications [31]. Finally, Unreal Engine [32], a game engine from Epic Games, has also been explored for its usability in space-based applications, close to terrain [33], and for proximity operations [34, 35].

In this work, a high-fidelity simulation environment for horizon-based OpNav is created using Blender. The steps involved in this development, from the selection of the rendering software, to the various considerations regarding the rendering process that impact the performance of OpNav, are discussed. This environment is used to render images of the Moon as seen by a fixed field of view camera, traveling along a baseline NRHO propagated in a full-ephemeris model. We highlight NRHO-specific considerations when using OpNav, particularly due to the large variation in perilune and apolune distances, as well as the geometric orientation of the orbit with respect to the Sun. The resulting images are processed by the non-iterative horizon-based OpNav algorithm from Christian and Robinson [36] to obtain position vector measurements. Insights on the impact of the various physical constraints as well, as engineering choices on the accuracy of the measurements are provided. Finally, the measurements are incorporated into a navigation filter to evaluate the state estimation performance relying solely on optical measurements.

The remainder of this paper is organized as follows: first, in Section 2, we provide an overview of the full-ephemeris dynamical model that is used to study NRHOs, as well as a brief discussion on NRHOs themselves. This is followed by Section 3, where we detail the Blender-based simulation setup that generates images for horizon-based OpNav. In Section 4, the horizon-based OpNav algorithm is reviewed, and considerations specific to employing this technique for navigation along an NRHO are discussed. Numerical results based on rendered images and the implemented OpNav algorithm are provided in Section 5. Finally, Section 6 provides concluding remarks.

2. **Spacecraft Model**

This section provides an overview of the full-ephemeris-based dynamical spacecraft model and introduces near rectilinear halo orbits.

2.1 *Equations of Motion*

Consider a spacecraft in cislunar space under the gravitational influence of the Moon, Earth, and Sun, a Moon-centered inertial frame F_I, and a lunar principal axes frame F_P. The equations of motion for the spacecraft are given by

$$\begin{aligned} \dot{\boldsymbol{r}} &= \boldsymbol{v}, \\ \dot{\boldsymbol{v}} &= -\frac{\mu}{r^3}\boldsymbol{r} + \boldsymbol{a}_{\mathrm{J2}} + \sum_i \boldsymbol{a}_{N_i} + \boldsymbol{a}_{\mathrm{SRP}}, \end{aligned} \tag{1}$$

where $\boldsymbol{r}$ is the position of the spacecraft with respect to an unforced particle collocated with the center of the Moon, $\boldsymbol{v} \triangleq \dot{\boldsymbol{r}}$ is the velocity of the spacecraft with respect to $\mathrm{F_I}$, μ is the standard gravitational parameter of the Moon, $r = \|\boldsymbol{r}\|$, $\boldsymbol{a}_{\mathrm{J2}}$ is the perturbing acceleration due to the dominant coefficient in the lunar spherical harmonic gravitational model, $\boldsymbol{a}_{N_i}$ is the acceleration on the spacecraft due to third-body $i \in \{\text{Earth, Sun}\}$, and $\boldsymbol{a}_{\mathrm{SRP}}$ is the perturbing acceleration due to solar radiation pressure (SRP). The accelerations in (1) represent the major predictable external forces acting on the spacecraft [37], and are given by

$$\boldsymbol{a}_{\mathrm{J2}} = -\frac{\mu}{r^3}\boldsymbol{T}_{\mathrm{I}}^{\mathrm{P}} \begin{bmatrix} x\frac{3}{2}J_2\left(\frac{R}{r}\right)^2\left(1-5\frac{z^2}{r^2}\right) \\ y\frac{3}{2}J_2\left(\frac{R}{r}\right)^2\left(1-5\frac{z^2}{r^2}\right) \\ z\frac{3}{2}J_2\left(\frac{R}{r}\right)^2\left(3-5\frac{z^2}{r^2}\right) \end{bmatrix}, \quad (2)$$

where $\boldsymbol{r}|_{\mathrm{P}} = [x, y, z]^T$ is the spacecraft's position vector resolved in $\mathrm{F_P}$, $\boldsymbol{T}_{\mathrm{I}}^{\mathrm{P}} \in \mathbb{R}^{3\times3}$ is the rotation matrix that transforms components of a vector resolved in $\mathrm{F_P}$ into the components of the same vector resolved in $\mathrm{F_I}$, R is the reference equatorial radius of the Moon, and J_2 is the coefficient of the J2 term;

$$\boldsymbol{a}_{N_i} = -\mu_i\left[\frac{\boldsymbol{r}_i}{r_i^3} + \frac{\boldsymbol{d}_i}{d_i^3}\right], \quad (3)$$

where $\boldsymbol{d}_i$ is the position of perturbing body i with respect to the Moon, $d_i = \|\boldsymbol{d}_i\|$, and $\boldsymbol{r}_i = \boldsymbol{r} - \boldsymbol{d}_i$ is the position of the spacecraft with respect to perturbing body i;

$$\boldsymbol{a}_{\mathrm{SRP}} = P_\odot\left(\frac{1\mathrm{AU}}{r_\odot}\right)^2\frac{C_r A}{m}\frac{\boldsymbol{r}_\odot}{r_\odot}, \quad (4)$$

where $\boldsymbol{r}_\odot = \boldsymbol{r} - \boldsymbol{d}_\odot$ is the position of the spacecraft with respect to the Sun, $\boldsymbol{d}_\odot$ is the position of the Sun with respect to the Moon, $r_\odot = \|\boldsymbol{r}_\odot\|$, $P_\odot$ is the SRP magnitude at 1 AU, C_r is the radiation pressure coefficient, A is the Sun-lit surface area of the spacecraft, and m is the spacecraft mass.

Table 1 summarizes the constant parameters of the dynamics, along with parameters of the SRP term for a hypothetical spacecraft.

2.2 *Near Rectilinear Halo Orbit*

When studying spacecraft motion in cislunar space, simplified dynamical models are often employed to obtain initial guesses for possible motions; one such model is the circular-restricted three-body problem (CR3BP), which assumes only the gravitational influences of the Earth and the Moon, corotating about their common barycenter on respective circular orbits. In the CR3BP, numerous families of periodic orbits may be numerically constructed; the NRHO of interest in this work is a member of the halo orbit family about the L2 point with a period corresponding to a 9:2 resonance with respect to the synodic period, where the spacecraft completes 9 revolutions for every 2 synodic periods, exhibiting nearly stable characteristics within the simplified CR3BP model.

While the analogous NRHO in the full-ephemeris model (1) becomes only quasi-periodic, the orbit still offers relatively high stability [38]. In addition, the orbit offers nearly eclipse-free motion, where the spacecraft remains outside of the Earth's penumbral shadow for most of the time. These features make this NRHO well-suited for the crewed space station in cislunar space. Figure 1 shows the trajectory of the full-ephemeris NRHO in the Earth-Moon rotating frame and the inertial J2000 frame $\mathrm{F_I}$ used in this work.

3. Simulation of Optical Measurement

The development process for a simulation environment of optical measurements is discussed in this section. We first provide an overview of the various software that were considered. Then, considerations for rendering images for the purpose of OpNav are highlighted; specifically, spacecraft navigation requires uniquely precise measurements, and care must be taken to properly configure the rendering software. This is followed by a description on the modeling of the imaged celestial body, sunlight, and any eclipsing body. Finally, piecing everything together, we provide a procedural guide on how such an environment may be used to generate horizon-based optical measurements.

3.1 *Comparison of Rendering Engines*

There are multiple rendering software that may be used for the purpose of simulating optical navigation. At the early stages of this work, we tested using either Blender or Unreal Engine 5 (UE5), and concluded that Blender was better-suited for the task at hand. We avoided POV-Ray due to the inactive development community. While the Basilisk/Vizard suite provides a ready-made set of functions for this purpose, we also opted against this option due to our need for customizability and control over the rendering process.

Table 1: Constants in full-ephemeris dynamics

Dynamics parameter	Value
Moon gravitational parameter μ, km^3/s^2	4902.800582147760
Earth gravitational parameter $\mu_\oplus$, km^3/s^2	398600.432896939
Sun gravitational parameter $\mu_\odot$, km^3/s^2	132712197035.766
Moon equatorial radius R, km	1737.4
Moon J_2	0.0002024
Astronomical unit, km	149597870.7
SRP magnitude at 1 AU $P_\odot$, N/m^2	4.56e-6
Radiation pressure coefficient C_r	1.15
SRP ballistic coefficient m/A, kg/m^2	500

When making the selection of rendering software, its interoperability with generic programming languages is critical, as it facilitates the simulation process that involves not only rendering images but also processing them and computing quantities that may rely on generic scientific routines. For this purpose, both Blender and UE5 have interfaces with Python, through which SPICE [39,40] routines, which is a system of data files and functions developed by the Navigation and Ancillary Information Facility at NASA's Planetary Science Division for space mission modeling, planning, and execution, as well as other third-party scientific libraries, may be called.

A fundamental difference between Blender and UE5 is the primary purpose of the respective software; Blender is a rendering engine, whose purpose is to render scenes accurately, while UE5 is a game engine, whose purpose is to rapidly render interactive scenes. Thus, while Blender has numerous settings that may improve the physical accuracy of the ray-tracing process at the cost of longer rendering times, UE5 has more emphasis on clever approximations that can be made to speed up the rendering of a scene that looks realistic to the human eye. While UE5's fast rendering speed is attractive for simulation, this comes at a cost of poor representation of edges, which is not visible to the naked eye by design, but becomes apparent when zooming in closely.

This is visible in Figure 2, which shows two example frames of the Moon rendered using Blender, Vizard, and Unreal Engine 5. The third row shows a zoomed-in view of the limb of the images in the second row. While both Blender and Vizard have a staircase pattern along the zoomed-in limb, shown on the bottom left and bottom center windows, the rendered image from UE5 contains irregular artifact pixels along the limb, as shown on the bottom right window. This effect led us to choose Blender over UE5 for the remainder of this work in order to be able to evaluate OpNav performance on NRHO under a well-understood simulation environment. Nevertheless, we note that while unnatural, the artifact from the UE5 image could also be interpreted as mimicking real image effects, where various types of noise in the image sensor can creep in. While this is beyond the scope of this work, it may also be reasonable to adopt UE5 for the simulation and study OpNav using these imperfect, arguably corrupted images.

3.2 *Rendering Considerations*

In order to simulate measurements for horizon-based OpNav, it is critical that the rendered image contains the lit limb of the imaged body at the physically accurate location. Caution is required when using rendering engines that are targeted for real-time applications, such as video games, as the Level of Details (LOD) setting on the software is typically tuned to sacrifice the physical accuracy of objects that are far from the camera (thus occupying fewer pixels within the image) in favor of rendering speed. This is visible in Figure 2 from the bottom right window, corresponding to the zoomed-in view of the lit limb from UE5. While the bottom left and bottom center windows, corresponding to the zoomed-in view of the lit limb from Blender and Unity, have a crisp "staircase" pattern along the limb, the image from UE5 has irregular rugged pixels along the limb, which is unnatural given that these images are rendered without terrain features.

In addition to LOD settings, two more considerations relating to rendering have an important influence on the accuracy of the generated measurements. The first is the level of anti-aliasing applied. Aliasing refers to the artifacts caused by the rendering process, which results in jagged lines being formed. In Blender, this is controlled via the set-

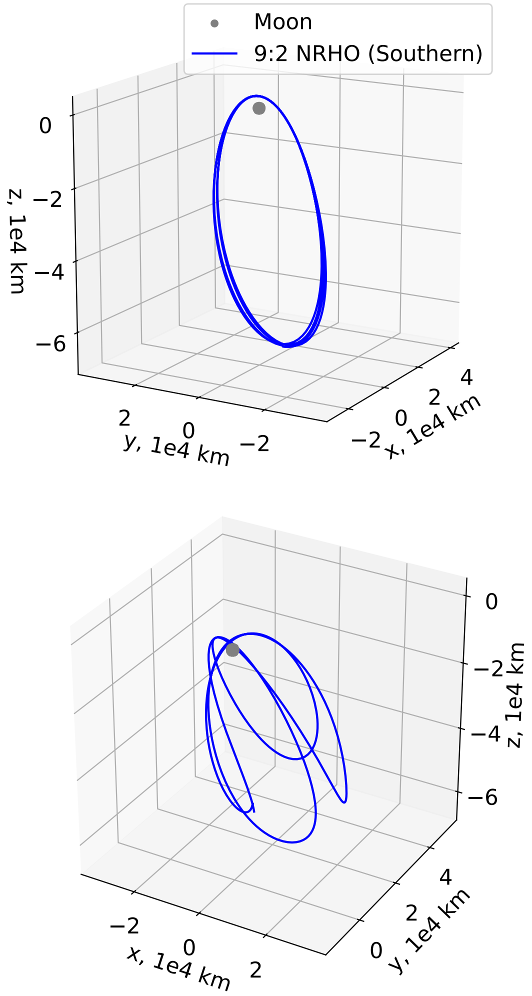

Fig. 1: Trajectory of Southern 9:2 resonant NRHO in the full-ephemeris model, shown in the Earth-Moon rotating frame (top) and the J2000 frame (bottom).

ting on `pixel filtering` [41]. Figure 3 shows the effect of the value of pixel filtering used when rendering the image of the Moon. While for the sake of horizon-based OpNav, a jagged limb is preferable, a "realistic" setting would be dependent on what the rendered image should simulate. A typical digital camera would have an anti-aliasing filter built-in, and therefore images produced by an off-the-shelf camera are likely to include anti-aliasing. On the other hand, if the camera is specifically configured for the purpose of OpNav, it is possible to assume that the anti-aliasing filter is removed, or the process is reversed through deconvolution. In this work, under the assumption that the spacecraft is equipped with an OpNav-purposed camera, the anti-aliasing is removed, by setting `pixel filtering` to 0.

The second is on the ceiling or flooring operation which the rendering software takes to determine whether a sufficient portion of the pixel is above a threshold value. Depending on the convention used by the software, the ceiling or flooring operation results in some pixels at the edge of the physical limb being falsely coloured, which averages out to the limb being shifted by 0.5 pixels, either towards the top left or the bottom right of the image. This effect is illustrated in Figure 4, taking as an example the case where the rendering software rounds up any pixel that contains a portion of the Moon's lit limb within it. Supposing that the pixel is not illuminated regardless of whether $< 50\%$ or $> 50\%$ of the pixel should be physically occupied by the lit limb, it is possible to see that the location of the actual limb would be portrayed in the image with a -0.5 pixel bias shift to the right. Hence, in this case, it would be appropriate to shift back any detected limb point by $+0.5$ pixel.

3.3 *Components in Simulation Environment*

In a minimal optical navigation simulation, the observed body and sunlight must be included. To augment the fidelity of the simulation, it is possible to consider the inclusion of the terrain of the observed body, along with any other neighboring celestial body that may cast a shadow on the observed body.

3.3.1 *Modelling the Observed Celestial Body*

Horizon-based OpNav algorithms work with ellipsoidal models for the observed body, which can be easily generated in rendering software. In the case of the Moon, since the reference ellipsoidal model as defined by the Planetary Constants Kernel (PCK) from SPICE has equal principal axes, it can be modelled as a sphere. In Blender, one option is to use a UV sphere, with a sufficient number of segments in the horizontal and vertical directions; in this work, 200 `segments` (vertical segments) and 100 `rings` (horizontal segments) are used. In addition, the "shade smooth" feature is applied to "change the way the shading is calculated across the surfaces (normals will be interpolated), giving the illusion of a smooth surface" [42].

To increase the fidelity of the simulation, the lunar terrain is introduced as a displacement of the mesh's surface with respect to the surface normal. In Blender, this is achieved by using the `Displacement Node` to the `material` of the mesh. The displacement can be computed from an elevation map of the celestial body; in this work, the dis-

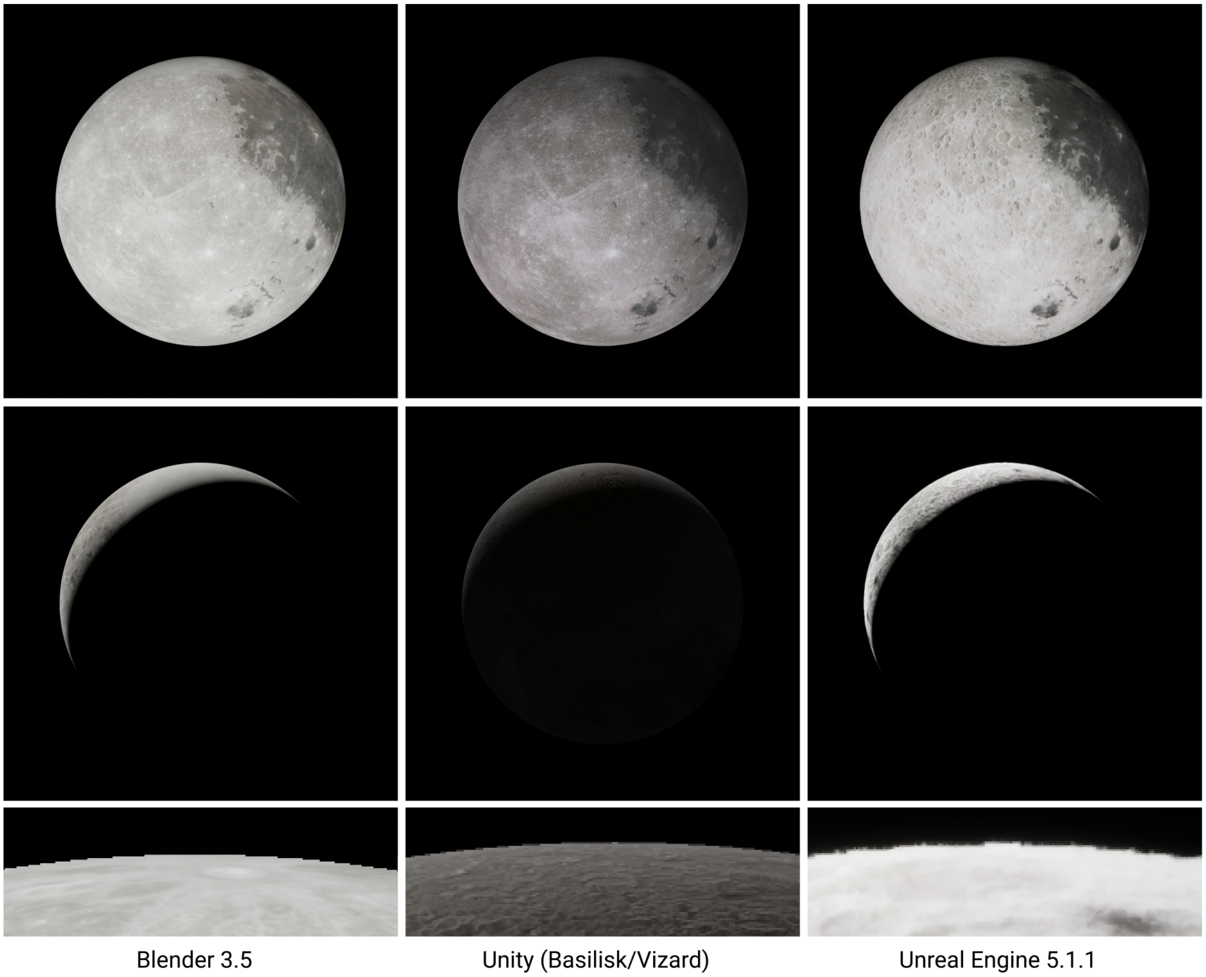

Fig. 2: Rendering comparison of the Moon. All images are taken using 2048 × 2048 pixels, and a field of view of 56.66° for the images in the first row, and 13.77° for images in the second row. The third row corresponds to a zoomed-in view on the top of the limb on the images in the second row. All images here are rendered without terrestrial features.

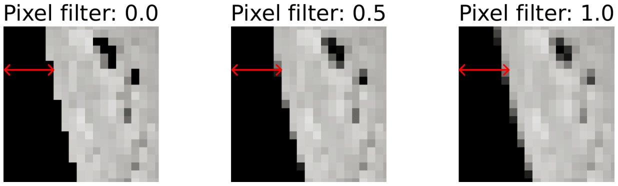

Fig. 3: Effect of pixel filtering on the lit limb of the Moon within the rendered image.

placement of the Moon obtained from the Lunar Orbiter Laser Altimeter (LOLA) instrument, provided by NASA, with a 64 pixels per degree resolution, is used [43].

The inclusion of terrain is particularly important when simulating horizon-based OpNav of the Moon; as reported by Christian [44], when a sub-pixel level edge finding technique (to be discussed in Section 4.2) is employed, the local terrain of the Moon becomes important as soon as the Moon's radius corresponds to about 48 pixels within the image. A strong proponent of this effect is the non-negligible discrepancy between the center of mass of the Moon and the geometric center of a triaxial ellipsoidal approximation of it; because the Moon is tidally locked, the far side of the Moon has experienced a significantly greater number of impact events, resulting in a far more rugged terrain than the near side. Since the OpNav algorithm relies on a triaxial ellipsoidal assumption of the observed celestial body, deviations of

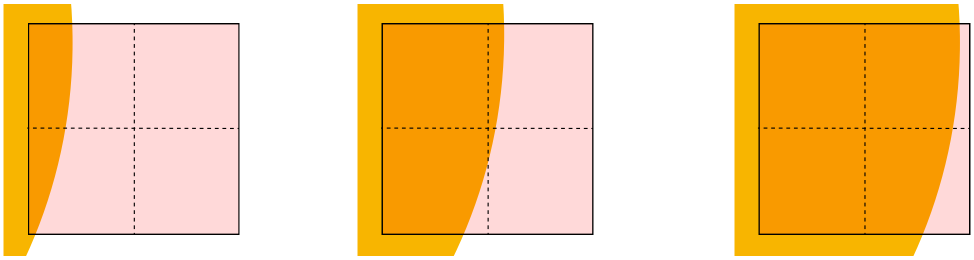

Lit limb occupying <50% of pixel

Lit limb occupying ~50% of pixel

Lit limb occupying >50% of pixel

Fig. 4: Illustration of ceiling/flooring operation taken by software when rendering pixels on the edge of the lit limb. Ideally, the pixel with the limb occupying $< 50\%$ should not be illuminated, while the pixel with the limb occupying $\geq 50\%$ should be.

the best-fitting ellipsoid have a direct impact on the algorithm's performance. While beyond the scope of this work, one may consider compensating for this deviation by incorporating corrective terms on the geometric center, dimensions, and orientation of the best-fitting ellipsoid, as reported in [45].

3.3.2 *Modelling Sunlight*

In typical spacecraft OpNav applications, due to the much larger distance to the Sun compared to the distance from the observed body to the spacecraft, sunlight can be well-approximated using a directional light source. This is preferable to placing a point light source, which can be prohibitive due to the difference of length scales that are involved. For example, in the cislunar case, the Sun-Moon distance is almost 10^5 times the radius of the Moon, making it impractical to place a point light source far into the distance while also having a sufficiently detailed mesh model for the Moon.

In reality, the Sun is a light source of finite volume. In Blender, the `Sun Light` object offers an `angle` variable, which dictates the angular diameter of the light source [46]. This becomes particularly important when modeling eclipses.

3.3.3 *Inclusion of Eclipsing Body*

When the Moon is within the shadow cast by the Earth, the Moon's limb becomes partially or entirely invisible to the spacecraft camera. While a total lunar eclipse typically lasts only about 30 minutes to an hour, the eclipse itself may last for a few hours. While its impact may be negligible on the long-term OpNav simulation of a cislunar spacecraft, it can be included to add fidelity to the simulation of operating a spacecraft around the epoch of a lunar eclipse. Figure 5 shows rendered images during the lunar eclipse on 2025-03-14 UTC on the top row, along with rendered images without the Earth (and therefore without a lunar eclipse) for comparison on the bottom row. During this eclipse, the Moon enters the Earth's penumbra at 03:57:28 UTC, the partial eclipse begins at 05:09:40 UTC, and the full eclipse begins at 06:26:06 UTC.

3.4 *Simulation Process*

When simulating optical measurements from a spacecraft, any arbitrary reference frame may be used to locate the spacecraft, sunlight, as well as any relevant celestial bodies. In the case of simulating images for horizon-based OpNav, a practical reference frame to use is the principal axes frame of the primary celestial body that is being imaged. By using the principal axes frame, the mesh of the primary celestial body does not need to be moved or rotated, thus simplifying the simulation process.

Using the principal axes frame, the high-level process for generating the optical measurement can be summarized by the following steps:

1. Create mesh of the primary celestial body, with its principal axes aligned with the xyz-directions of the rendering environment;

2. Query position of the Sun $\boldsymbol{r}_{\odot}$ in the principal axes frame from SPICE ephemeris data;

3. Create directional light with angle based on $\boldsymbol{r}_{\odot}$;

4. Query position of any additional celestial bodies that may cast a shadow on the imaged body from SPICE and place a mesh at this position;

5. Place the camera's position and orientation based on the spacecraft's position and attitude.

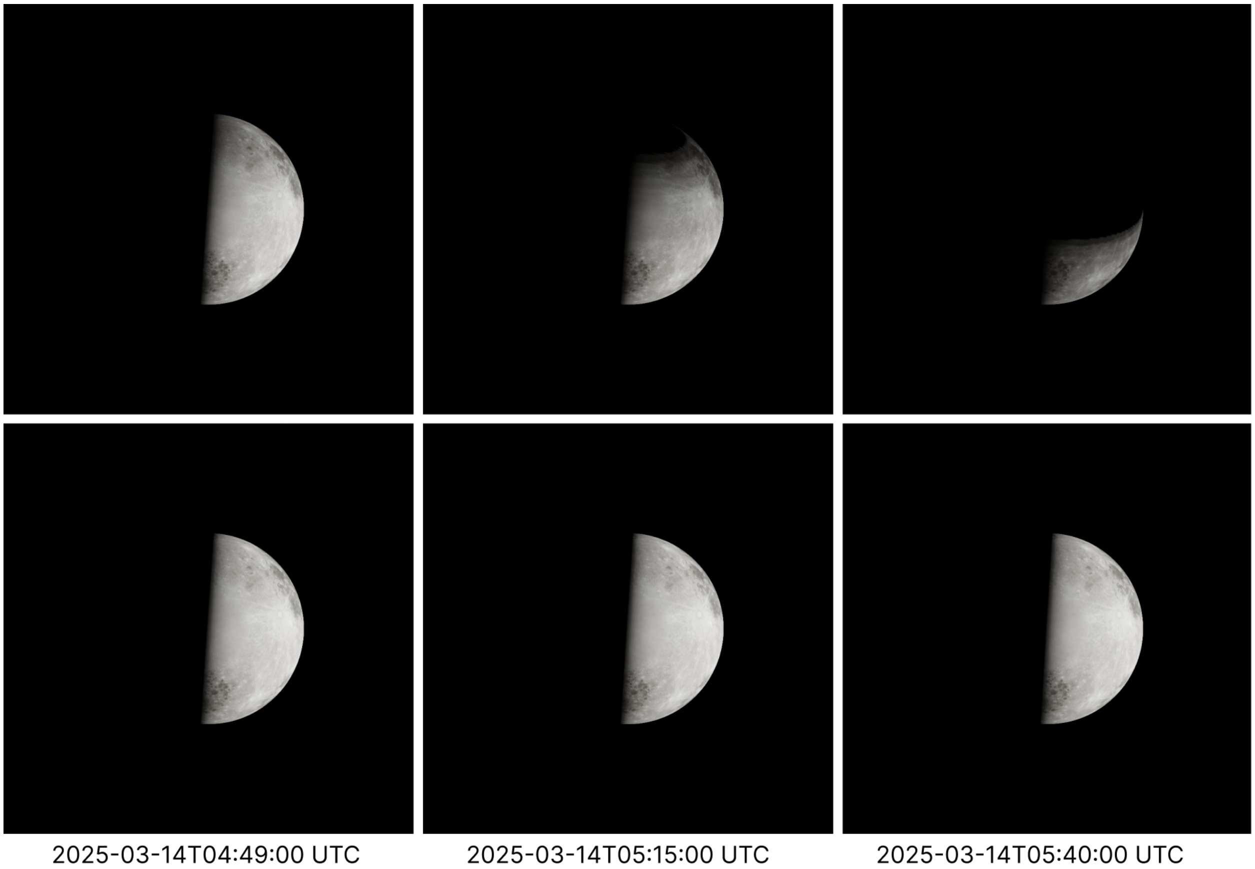

Fig. 5: Effect of lunar eclipse during the total eclipse on 2025-03-14 UTC, visualized from position vector $[0, 0, -25000]$ km in the Moon principal axes frame. The images in the top row are rendered in a Blender environment that includes the Earth, while images in the bottom row are rendered in an environment that does not, for comparison. The image on the top left corresponds to a penumbral eclipse, while the images on the top center and right correspond to partial lunar eclipses.

Once a rendering environment is initialized, a new measurement may be obtained by going through steps 2 through 5.

4. Horizon-Based Optical Navigation on NRHO

Various state estimation problems can be posed in the context of horizon-based OpNav, depending on the unknowns [17]. In this work, we consider the problem with known spacecraft attitude and unknown spacecraft position. This is a relevant and realistic scenario when considering autonomous spacecraft navigation, since conventional sensors, such as star trackers, can provide attitude information to high precision [17, 47]. Specifically, we consider the Christian-Robinson algorithm [36] due to its noniterative, high-performing characteristics, as previously reported in the literature [17, 36, 44, 48].

4.1 *Overview of Christian-Robinson Algorithm*

In this work, the singular value decomposition (SVD)-based variant of the non-iterative OpNav algorithm, as described by Christian [44], is employed. The reader is directed to the literature [17, 44, 48] for an in-depth discussion of the brief summary that follows. Note that hereafter, the word *planet* is used to denote a planetary body, which also includes planetary moons, provided that they can be well-approximated as an ellipsoidal body.

4.1.1 *Position Estimate from Limb Points*

Let the camera frame $\mathrm{F_C}$ be defined with the z-axis aligned with the boresight of the camera, and the xy-plane lying on the image plane of the camera. Furthermore, consider a set of m detected limb points, given as pairs of pixel coordinates $\{u_i, v_i\}_{i=1}^m$. These pixel coordinate points can be related to a vector $\boldsymbol{s}_i$ in the image plane via

$$\boldsymbol{s}_i = \begin{bmatrix} x_i \\ y_i \\ 1 \end{bmatrix} = \boldsymbol{K}^{-1} \begin{bmatrix} u_i \\ v_i \\ 1 \end{bmatrix}, \tag{5}$$

where $\boldsymbol{K}$ is the intrinsic camera calibration matrix [17,44,49]. Note that $u_i, v_i \in \mathbb{R}$, since the limb points may be detected at sub-pixel level precision; this will be discussed in further detail in a subsequent subsection.

Then, the vector $\boldsymbol{n} \in \mathbb{R}^3$ pointed from the spacecraft camera to the center of the body in the camera frame is obtained by solving the least-squares problem

$$\boldsymbol{H}\boldsymbol{n} = \boldsymbol{1}_{m\times 1}, \tag{6}$$

where

$$\boldsymbol{H} = \begin{bmatrix} \bar{\boldsymbol{s}}_1^T/\|\bar{\boldsymbol{s}}_1\| \\ \vdots \\ \bar{\boldsymbol{s}}_m^T/\|\bar{\boldsymbol{s}}_m\| \end{bmatrix} = \begin{bmatrix} \bar{\boldsymbol{s}}_1'^T \\ \vdots \\ \bar{\boldsymbol{s}}_m'^T \end{bmatrix}, \tag{7}$$

and $\bar{\boldsymbol{s}}_i$ is the i^{th} observed limb point on the image plane which relates to the coordinates in the image plane by

$$\bar{\boldsymbol{s}}_i = \boldsymbol{Q}\boldsymbol{T}_{\text{P}}^{\text{C}}\boldsymbol{s}_i, \tag{8}$$

where

$$\boldsymbol{Q} = \text{diag}(1/a, 1/b, 1/c), \tag{9}$$

with a, b, and c corresponding to the lengths of the planet's principal axes, and $\boldsymbol{T}_{\text{P}}^{\text{C}} \in \mathbb{R}^{3\times 3}$ is the rotation matrix from the camera frame to the planet's principal axes frame, which is assumed to be known with known spacecraft attitude. In this work, $\boldsymbol{T}_{\text{P}}^{\text{C}}$ is assumed to be given by

$$\boldsymbol{T}_{\text{C}}^{\text{P}} = \begin{bmatrix} \boldsymbol{b}_1 & \boldsymbol{b}_2 & \boldsymbol{b}_3 \end{bmatrix}, \tag{10}$$

where

$$\begin{aligned} \boldsymbol{b}_1 &= \boldsymbol{r} \times \boldsymbol{v}/\|\boldsymbol{r} \times \boldsymbol{v}\|, \\ \boldsymbol{b}_3 &= -\boldsymbol{r}/\|\boldsymbol{r}\|, \\ \boldsymbol{b}_2 &= \boldsymbol{b}_3 \times \boldsymbol{b}_1. \end{aligned} \tag{11}$$

Note that the Moon specifically is a degenerate case where the commonly used ellipsoidal model is a sphere with $a = b = c = R = 1737.4$ km.

The position vector of the spacecraft's camera in the camera frame, $\hat{\boldsymbol{r}}_{\text{C}}$, is obtained by

$$\hat{\boldsymbol{r}}_{\text{C}} = -(\boldsymbol{n}^T\boldsymbol{n} - 1)^{(1/2)}\boldsymbol{T}_{\text{C}}^{\text{P}}\boldsymbol{Q}^{-1}\boldsymbol{n}, \tag{12}$$

where $\boldsymbol{T}_{\text{C}}^{\text{P}} \in \mathbb{R}^{3\times 3}$ is the rotation matrix from the planet's principal axes frame to the camera frame. Finally, the position vector in the planet's frame can be obtained via the simple transformation

$$\hat{\boldsymbol{r}}_{\text{P}} = \boldsymbol{T}_{\text{P}}^{\text{C}}\hat{\boldsymbol{r}}_{\text{C}}. \tag{13}$$

4.1.2 *Measurement Covariance Model*

The measurement covariance associated with the Christian-Robinson algorithm using the Cholesky factorization is provided in [48]. Here, its adaptation to the SVD-based algorithm is provided.

The covariance of the least-squares problem solution $\boldsymbol{n}$ is given by

$$\boldsymbol{P}_n = [\boldsymbol{H}^T \,\text{diag}(1/\sigma_{y_1}^2, \ldots, 1/\sigma_{y_m}^2)\boldsymbol{H}]^{-1}, \tag{14}$$

where

$$\sigma_{y_i} = \boldsymbol{J}_i\boldsymbol{Q}\boldsymbol{T}_{\text{P}}^{\text{C}}\boldsymbol{R}_s\boldsymbol{T}_{\text{C}}^{\text{P}}\boldsymbol{Q}^T\boldsymbol{J}_i^T, \tag{15}$$

$\boldsymbol{R}_s$ is the covariance of the horizon measurements, and

$$\boldsymbol{J}_i = \frac{1}{\|\bar{\boldsymbol{s}}_i\|}\boldsymbol{n}^T(\boldsymbol{I}_{3\times 3} - \bar{\boldsymbol{s}}_i'\bar{\boldsymbol{s}}_i'^T). \tag{16}$$

As highlighted by Christian [48, 50], $\boldsymbol{R}_s$ can be approximated by the relation

$$\boldsymbol{R}_s \approx \left(\frac{\sigma_{\text{pix}}}{d_x}\right)^2 \begin{bmatrix} 1 & 0 & 0 \\ 0 & 1 & 0 \\ 0 & 0 & 0 \end{bmatrix}, \tag{17}$$

where σ_{pix} is the standard deviation of the observed horizon points in units of pixels, and d_x is the pixel pitch in terms of radians, as defined in [17, 48].

Then, using $\boldsymbol{P}_n$ from equation (14), the covariance of the position estimate in the camera frame is given by

$$\boldsymbol{P}_{\boldsymbol{r}_{\text{C}}} = \boldsymbol{F}\boldsymbol{P}_n\boldsymbol{F}^T, \tag{18}$$

where

$$\boldsymbol{F} = -(\boldsymbol{n}^T\boldsymbol{n} - 1)^{-(1/2)}\boldsymbol{T}_{\text{C}}^{\text{P}}\boldsymbol{Q}^{-1}\left(\boldsymbol{I}_{3\times 3} - \frac{\boldsymbol{n}\boldsymbol{n}^T}{\boldsymbol{n}^T\boldsymbol{n} - 1}\right). \tag{19}$$

The measurement covariance of the position in the planet's frame is finally obtained via

$$\boldsymbol{P}_{\boldsymbol{r}_{\text{P}}} = \boldsymbol{T}_{\text{P}}^{\text{C}}\boldsymbol{P}_{\boldsymbol{r}_{\text{C}}}\boldsymbol{T}_{\text{C}}^{\text{P}}. \tag{20}$$

The value for σ_{pix} is a critical quantity that dictates the measurement covariance. While in the case of a real image, σ_{pix} can be estimated from the camera's point spread function (PSF), this is not available for rendered images as is the case in this work. Instead, in this work, an approximate value for σ_{pix} is obtained by converting the limb point coordinates $\{u_i, v_i\}_{i=1}^m$, to a polar representation $\{\rho_i, \theta_i\}_{i=1}^m$ with respect to the image center (u_p, v_p). This process assumes the camera's boresight is aligned with the center of the imaged body. Note that this assumption is merely used to obtain an approximate value for σ_{pix}, but the position estimate $\hat{\boldsymbol{r}}_{\text{C}}$ from the OpNav

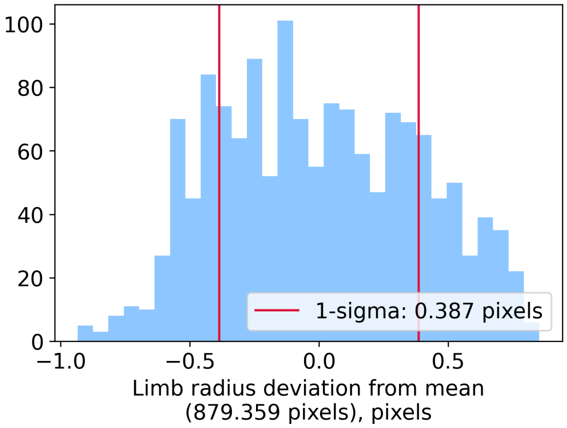

Fig. 6: Example distribution of radial components of limb points, ρ_i, from a rendered image

algorithm is obtained solely through equation (12), and does not make use of this assumption. Once the polar coordinate representations of the limb points are obtained, σ_{pix} is approximated as the standard deviation of the radii ρ_i.

4.2 *Detection of Lit Limb*

As described in the previous subsection, the horizon-based OpNav necessitates a set of limb points $\{u_i, v_i\}_{i=1}^m$. The detection of the lit limb consists of three principal steps, as outlined in [44]. The first step consists of detecting the limb at the pixel level using the Canny edge detection algorithm [51]. This is followed by filtering these detected points based on the illumination direction within the image plane, and finally a sub-pixel level refinement of the filtered pixel-level limb points.

For the first step, various edge detectors can be used, and a comparative assessment is provided in [44] for the interested reader. The second step consists of scanning the image along the direction of the sunlight projected onto the image, which is obtained by

$$\boldsymbol{u}'_{\text{illum}} = \frac{\boldsymbol{u}_{\text{illum}}}{\|\boldsymbol{u}_{\text{illum}}\|}, \tag{21}$$

where

$$\boldsymbol{u}_{\text{illum}} = -\begin{bmatrix} 1 & 0 & 0 \\ 0 & 1 & 0 \end{bmatrix} \boldsymbol{T}_{\text{C}}^{\text{P}} \boldsymbol{d}_{\odot}, \tag{22}$$

Note that $\boldsymbol{d}_{\odot}$ is known from planetary ephemerides alone, irrespective of knowledge of the spacecraft's position. Along each scan, the first pixel with a pixel intensity higher than a pre-defined threshold ϵ is recorded as a "coarse" limb point. Based on these coarse limb points, an n_v-by-n_u binary masking matrix $\boldsymbol{M}$ is constructed; $\boldsymbol{M}$ has 1's on n_M-by-n_M submatrices centered at the coarse limb point coordinates, and zeros elsewhere. Note $n_M < n_v$, $n_M < n_u$, and n_M must be odd. In this work, a threshold of $\epsilon = 20$ and $n_M = 5$ is used. Once $\boldsymbol{M}$ is constructed, the Hadamard product of $\boldsymbol{M}$ and the Canny edge pixels in matrix form returns the filtered edge pixels near the coarse limb points. The final refinement is done using the Zernike moment-based technique described in [44]. This involves computing a corrective term on the filtered pixel-level edge coordinates, $\{\tilde{u}_i, \tilde{v}_i\}_{i=1}^m$, based on the Zernike moment information of a local, N-by-N patch centered at $\{\tilde{u}_i, \tilde{v}_i\}_{i=1}^m$. The expression for the final sub-pixel level edge, $\{u_i, v_i\}_{i=1}^m$, is given by

$$\begin{bmatrix} u_i \\ v_i \end{bmatrix} = \begin{bmatrix} \tilde{u}_i \\ \tilde{v}_i \end{bmatrix} + \frac{Nl}{2} \begin{bmatrix} \cos\psi \\ \sin\psi \end{bmatrix}, \tag{23}$$

where

$$\psi = \text{atan2}(\text{Im}(A_{11}), \text{Re}(A_{11})), \tag{24}$$

$$l = \left[1 - w^2 - \sqrt{\left(w^2 - 1\right)^2 - 2w^2 A_{20}/A'_{11}}\right] / w^2. \tag{25}$$

Here, w is the width parameter, set to 0.5 in this paper, and A_{nm} are Zernike moments of the original image, whose expressions are given in [44].

Figure 7 shows the resulting limb points from the three steps. With the Canny edge detection alone, craters casting sharp shadows on the lunar surface are falsely identified, as shown by the red points. The illumination scans, shown by the orange lines, run from the top left to the bottom right along the sunlight direction and return the "coarse" limb points shown by the blue stars. Applying a 5-by-5 mask around each coarse limb point, the Zernike moment-based sub-pixel edge refinement is applied, to finally obtain the lime green points.

4.3 *NRHO-Specific Considerations for OpNav*

There are considerations for using OpNav specifically on NRHO that warrant attention. Firstly, the large variation in range, at around 3300 km around perilune and around 70,000 km around apolune for a 9:2 NRHO, poses a challenge in terms of choosing one (or multiple) appropriate camera(s). In addition, the orientation of the NRHO consisting of its apolune lobe extending below the Moon's pole (in the case of the Southern L2 NRHO, extending below the South pole) results in illumination conditions with a periodic structure.

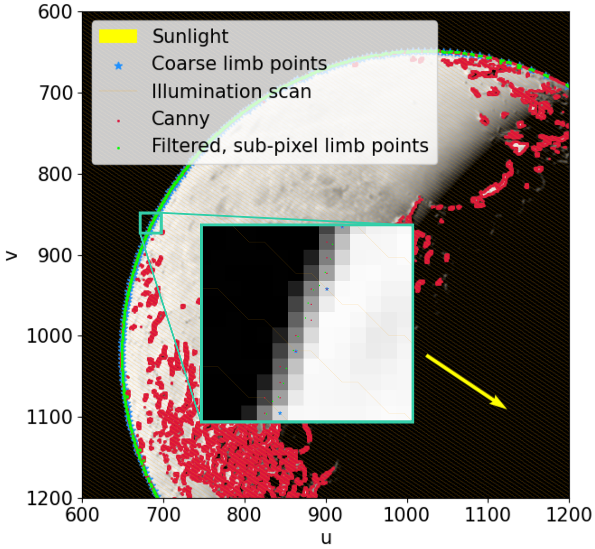

Fig. 7: Limb points detected on a rendered image of the Moon with terrain features. Crater limbs are identified by the Canny edge detector (shown in red) but are filtered out by applying a mask based on the coarse limb points (shown in blue). The lime green points correspond to sub-pixel level edges obtained based on the filtered, pixel-level edge from the Canny detector. The faded effect around the limb is due to the Gaussian blur that is applied to the raw rendered image.

4.3.1 *Variation of Distance to the Moon*

The range from the spacecraft camera to the observed body is a critical parameter that one must keep in mind when considering OpNav-based measurements. A critical issue for the horizon-based OpNav lies in the decreasing observability with range. To illustrate this, consider the apparent angular diameter of the Moon, $\delta_☾$, as a function of the range r. Through simple geometry, the expression for $\delta_☾$ can be obtained as

$$\delta_☾ = 2 \arctan\left(\frac{R_☾}{\sqrt{r^2 - R_☾^2}}\right), \tag{26}$$

where $R_☾ = 1737.4\,\text{km}$ is the radius of the Moon. Figure 8 shows this relationship for a range between 3,000 km and 75,000 km. Due to the nature of the expression (26), the apparent angular diameter rapidly falls with increasing ranges under 10,000 km, then tapers off with a much slower decrease at ranges over 10,000 km. This results in two complications vis-a-vis OpNav: due to the variation of an "ideal" field of view (FOV) camera at different ranges from the Moon, and due to the fundamental reduction of the observability of the range at larger distances.

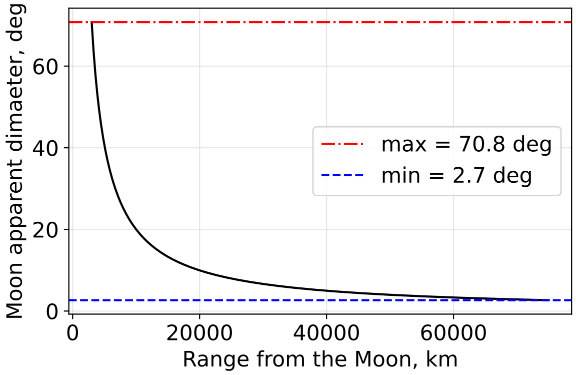

Fig. 8: Apparent diameter of the Moon against range

Since OpNav involves solving the least-squares problem from the limb pixel coordinates, it is preferable to have the Moon occupying a significant portion of the image. Near apolune of an NRHO, this would correspond to a small FOV of a few degrees; however, as the spacecraft approaches its perilune, an increasingly larger FOV is required for the Moon to fit within the image. Hence, while this is outside of the scope of this work, one may consider using multiple cameras to be operated at different range bands, or a variable FOV camera, in order to provide the ideal images to the OpNav algorithm.

The observability issue is more fundamental to the limb-based, range-finding problem; this is governed primarily by the mathematical expression (26), and cannot be circumvented. Rather, this pushes operation planning to prioritize collecting images for OpNav closer to the Moon, where the observability in the range is better, over collecting images further away.

4.3.2 *Variation of Illumination Condition*

The illumination condition of the Moon, when observed from an NRHO, varies between full Moons, half Moons, to new Moons, through a predictable pattern. Neglecting Earth eclipses, since the apolune of the NRHO is located at about 70,000 km below the south pole of the Moon, a half Moon is visible at any time around apolune. In contrast, when approaching perilune, the lighting condition on the Moon varies depending on the pass; if the Moon is at its closest or furthermost point from the Sun along its orbit around the Earth, the camera sees about half of the Moon throughout its perilune pass. Meanwhile, if the Moon is precisely at the halfway point between the closest and furthermost point from the Sun along its orbit,

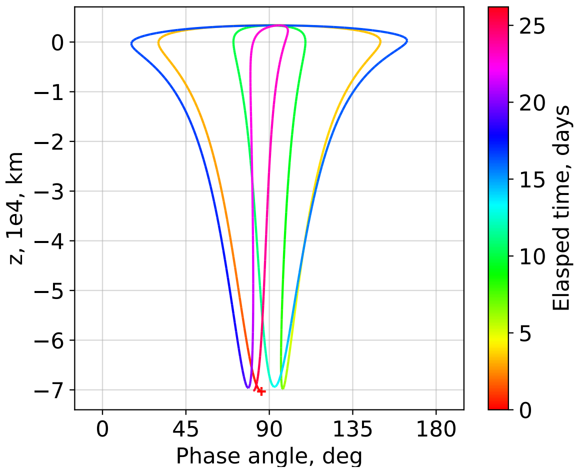

Fig. 9: z-position in the Earth-Moon rotating frame against phase angle $\phi_\odot$ along an NRHO over a duration of approximately 4 periods. The red cross indicates the z-position and phase angle at the initial time.

the spacecraft sees a switch between a full Moon and a new Moon through its perilune pass.

The variation in illumination condition along the NRHO is quantified through the phase angle (Sun-Moon-spacecraft angle) $\phi_\odot$, given by

$$\phi_\odot = \arccos\left(\frac{\boldsymbol{r}\cdot\boldsymbol{d}_\odot}{\|\boldsymbol{r}\|\|\boldsymbol{d}_\odot\|}\right). \tag{27}$$

This angle is shown against the z-coordinate along the NRHO in the Earth-Moon rotating frame in Figure 9, for a duration of approximately 4 periods. In this Figure, perilunes occur when z is at its largest value along each revolution, while the apolunes occur when z is at its most negative value along each revolution. As explained in the previous paragraph, $\phi_\odot$ is centered around 90° around apolunes, while a periodic fluctuation trend is observed around perilunes; specifically, tracking the trace from the initial time at apolune, the initial perilune involves flying from the Sun-lit side (small $\phi_\odot$) to the dark side (large $\phi_\odot$), as shown by the yellow trace, while the next perilune flies over the terminator, resulting in $\phi_\odot \approx 90°$ throughout, as shown by the light green trace. The perilune flying over the Sun-lit/dark side and over the terminator alternates, as expected.

4.4 *Navigation Filter*

The operation of a spacecraft requires a navigation filter to provide an estimate of the spacecraft's state given a sequence of OpNav measurements. For this purpose, we implement an extended Kalman filter (EKF) [52]. This recursive filtering technique has seen great popularity and success throughout the history of spaceflight [53], primarily due to its simplicity and low computational burden. In this section, we follow the notation in [22] and let $\boldsymbol{\theta} = [\boldsymbol{r}|_{\mathrm{I}}^T, \boldsymbol{v}|_{\mathrm{I}}^T]^T$ denote the spacecraft's state, evolving by (1) as $\dot{\boldsymbol{\theta}} = f(t,\boldsymbol{\theta})$. The EKF is implemented in discrete time $\{t_j \in \mathbb{R} : t_{j+1} > t_j, j \in \mathbb{N}\}$, and we write the (marginal) filtering posterior of the state vector $\boldsymbol{\theta}_a = \boldsymbol{\theta}(t_a)$ given a sequence of measurements $\{\boldsymbol{y}_k\}_{k=0}^b$ by the probability density function $p(\boldsymbol{\theta}_a|\{\boldsymbol{y}_k\}_{k=0}^b) = \mathcal{N}(\hat{\boldsymbol{\theta}}_{a|b}, \boldsymbol{\Sigma}_{a|b})$. The filter updates the estimates recursively from a Gaussian prior $\mathcal{N}(\hat{\boldsymbol{\theta}}_{0|0}, \boldsymbol{\Sigma}_{0|0})$ in a time prediction followed by a measurement update, described separately below.

4.4.1 *Time Prediction*

To account for uncertainties in (1) we include additive process noise [52], resulting in the time update

$$\hat{\boldsymbol{\theta}}_{j|j-1} = \hat{\boldsymbol{\theta}}_{j-1|j-1} + \int_{t_{j-1}}^{t_j} f(\tau, \hat{\boldsymbol{\theta}}_{j-1}(\tau))\mathrm{d}\tau, \tag{28}$$

$$\boldsymbol{\Sigma}_{j|j-1} = \boldsymbol{\Phi}(t_j, t_{j-1})\,\boldsymbol{\Sigma}_{j-1|j-1}\boldsymbol{\Phi}(t_j, t_{j-1})^T + \boldsymbol{Q}_j, \tag{29}$$

where (28) is evaluated using an explicit embedded Runge-Kutta Prince-Dormand (8,9) method from the GNU scientific library [54], and $\boldsymbol{\Phi}(t_j, t_{j-1})$ is the state-transition matrix obtained by numerically integrating the initial value problem

$$\begin{cases} \dot{\boldsymbol{\Phi}}(\tau, t_{j-1}) = \left(\left.\dfrac{\partial f(t,\boldsymbol{\theta})}{\partial \boldsymbol{\theta}}\right|_{(\tau,\hat{\boldsymbol{\theta}}_{j-1}(\tau))}\right)\boldsymbol{\Phi}(\tau, t_{j-1}), \\ \boldsymbol{\Phi}(t_{j-1}, t_{j-1}) = \boldsymbol{I}_{6\times 6}. \end{cases} \tag{30}$$

The process noise is modeled as an unbiased random process, and its covariance $\boldsymbol{Q}_j$ is taken to be a function of the sample period $h_j = t_j - t_{j-1}$, as

$$\boldsymbol{Q}_j = \sigma_u^2 \begin{bmatrix} \frac{1}{3}h_j^3 & \frac{1}{2}h_j^2 \\ \frac{1}{2}h_j^2 & h_j \end{bmatrix}, \tag{31}$$

where σ_u^2 is the diffusion coefficient to be adjusted to optimize the filter performance [55].

4.4.2 *Measurement Update*

The OpNav measurements are modeled as direct position measurements with additive Gaussian noise

$$\boldsymbol{y}_j = \boldsymbol{E}\boldsymbol{\theta}_j + \boldsymbol{r}_j, \quad \boldsymbol{r}_j \sim \mathcal{N}(\boldsymbol{0}, \boldsymbol{R}_j), \quad \boldsymbol{E} = \begin{bmatrix}\boldsymbol{I} & \boldsymbol{0}\end{bmatrix}, \tag{32}$$

resulting in the linear standard measurement update

$$\boldsymbol{K}_j = \boldsymbol{\Sigma}_{j|j-1}\boldsymbol{E}^T \left(\boldsymbol{E}\boldsymbol{\Sigma}_{j|j-1}\boldsymbol{E}^T + \boldsymbol{R}_j\right)^{-1}, \tag{33}$$

$$\hat{\boldsymbol{\theta}}_{j|j} = \hat{\boldsymbol{\theta}}_{j|j-1} + \boldsymbol{K}_j \left(\boldsymbol{y}_j - \boldsymbol{E}\hat{\boldsymbol{\theta}}_{j|j-1}\right), \tag{34}$$

$$\boldsymbol{\Sigma}_{j|j} = \left(\boldsymbol{I} - \boldsymbol{K}_j\boldsymbol{E}\right)\boldsymbol{\Sigma}_{j|j-1}. \tag{35}$$

Both the measurement $\boldsymbol{y}_j$ and the measurement noise covariance $\boldsymbol{R}_j$ are direct outputs of the OpNav algorithm, in (13) and (20), respectively.

5. Experiments

The OpNav simulation framework is used to generate images along an NRHO and run the Christian-Robinson algorithm to construct position measurements with associated measurement covariance. The measurements are then incorporated into an EKF.

The camera is considered to have an image size of 2048-by-2048 pixels, with a focal length $f = 240$ mm and a sensor size $s = 100$ mm along each direction, which corresponds to FOV of about 23.54°. As shown by Figure 8, this camera can thus image the full Moon at ranges above ∼8500 km. To account for operational considerations on pointing the camera, images are generated at ranges equal to or above 10,000 km. The detector array skewness in the camera calibration matrix $\boldsymbol{K}$, as defined in [17,44], is set to 0.

An image is rendered at 6-hour intervals along a baseline NRHO; if the spacecraft is closer than 10,000 km, the measurement is skipped and the spacecraft state is propagated for another 6 hours until the next measurement. This results in 291 imaging opportunities along the NRHO for a duration of about 75 days.

5.1 *Effect of Rendering Settings*

Figure 10 shows the effect of anti-aliasing as well as the half-pixel compensation. All images are generated without terrain. Since Blender floors the pixels during the rendering process, the half-pixel compensation corresponds to applying a +0.5 pixel shift should be applied on all limb points $\{u_i, v_i\}_{i=1}^m$. The statistics from each set of measurements are given in Table 2.

The effect of anti-aliasing is visible by comparing Figures 10a and 10b. The most notable difference is in the slight positive bias in the camera z-direction when anti-aliasing is included. The anti-aliasing causes the apparent diameter to deviate from the true, crisp, jagged limb from an image without anti-aliasing; this results in the boresight bias that is visible in (b). Indeed, the mean error in the z-direction is about 6 times worse when anti-aliasing is used, while the standard deviation is marginally better with anti-aliasing. The latter observation may be attributed to the jagged nature of images without anti-aliasing, which hinders the sub-pixel edge correction step that uses the local Zernike moments about the pixel-level edge; the effect is only marginal due to the Gaussian blur that is applied prior to the edge detection process.

The half-pixel compensation results in the difference observed by comparing 10a and 10c. Since the pixel shift simply moves the Moon uniformly within the image, it results in no discernible difference in the camera frame's z-direction (boresight). Meanwhile, in the other two directions, omitting the 0.5 pixel shift results in biased $\hat{\boldsymbol{r}}_{\mathrm{C}}$. It is possible to validate the effect of this pixel shift as follows: since the image contains 2048 pixels in each direction, the physical distance represented within a single pixel at a range of 70,000 km can be computed from the focal length f and the sensor size s as $100 \times 70000/240 \approx 14\,\mathrm{km}$. If the Moon is shifted by half of a pixel from its true position, we should expect a bias of about 7 km at a range of 70,000 km, which coincides with what we can observe in 10c.

5.2 *Effect of Terrain*

The effect of the lunar terrain as displacement on the ellipsoidal mesh is observed in Figure 11, where the measurements are generated from images with terrain, without anti-aliasing, and with half-pixel compensation. This may be compared against 10a, which uses the same settings apart from omitting the terrain. Note that, unlike the half-pixel shift, the terrain alters the dimensions and orientation of the best-fitting ellipsoid from the model that is given to the Christian-Robinson algorithm via equation (9). Recall that in this work, a spherical Moon model based on values from PCK is used; modifying the triaxial model's dimensions and orientation based on recent lunar geodetic data may reduce the error due to terrain. The error on $\hat{\boldsymbol{r}}_{\mathrm{C}}$ appears on all three components. Looking at the last row in Table 2, it is possible to see that both the mean and standard deviation of the measurement errors worsen with terrain in all components.

5.3 *Comparison of Observability per Camera-Frame Component*

Across all cases in Figure 10 and 11, it is possible to observe that the error in the camera z-direction is

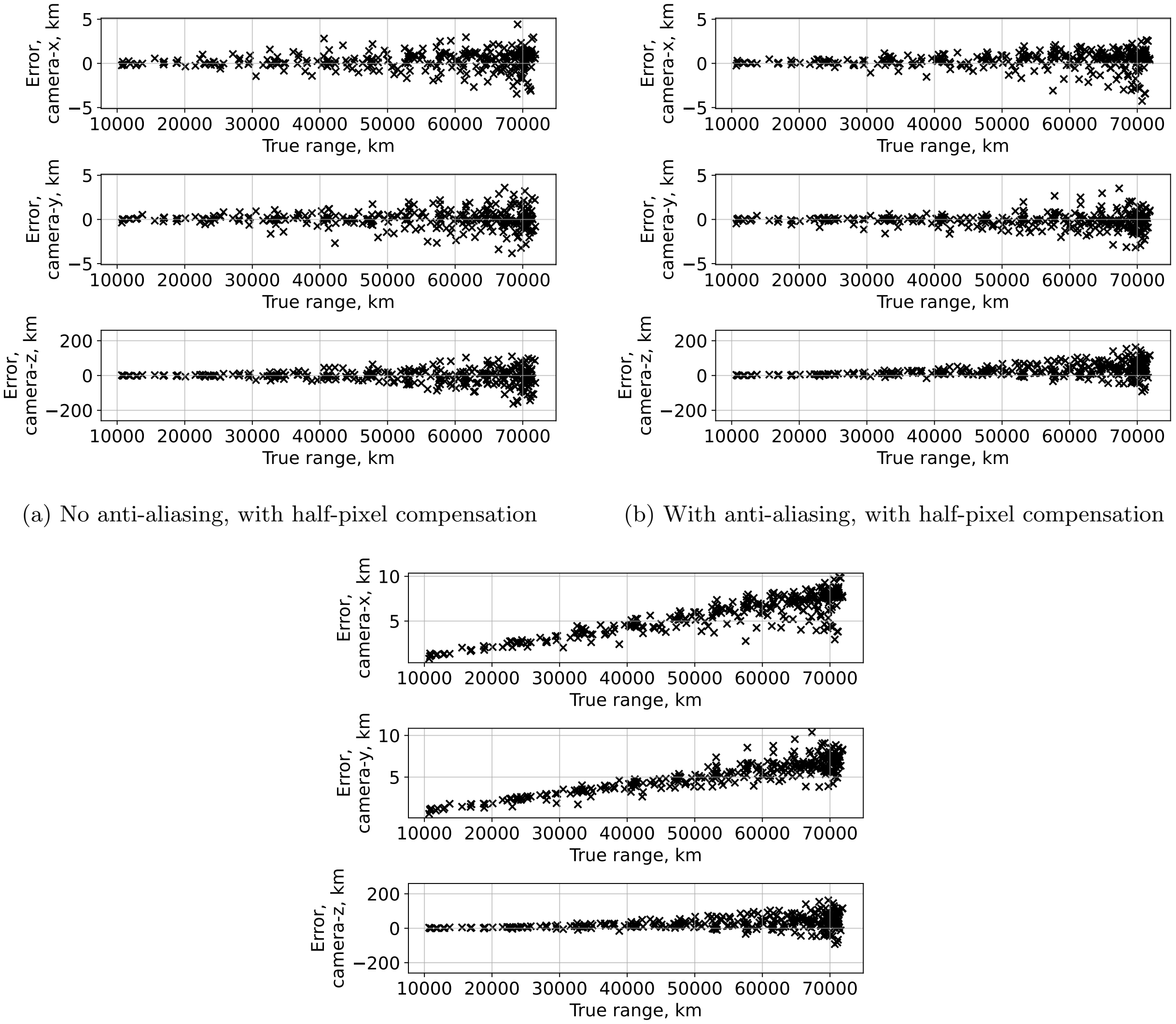

(a) No anti-aliasing, with half-pixel compensation

(b) With anti-aliasing, with half-pixel compensation

(c) With anti-aliasing, without half-pixel compensation

Fig. 10: Effect of rendering settings on position measurement error in the camera frame, shown against range from the Moon. All three images are rendered without terrain.

about two orders of magnitude worse than in the x- and y-directions. This is a manifestation of the difference in observability along the camera boresight compared to the directions on the plane perpendicular to the boresight. Since the apparent diameter of the Moon varies slowly as the range increases, the observability in this direction is poorer than in the other two directions.

Also, in all three components, a smaller range corresponds to the Moon occupying a bigger portion of the image, generally resulting in a greater number of limb points m. Particularly for the (Southern) NRHO, since at ranges beyond 10,000 km the spacecraft is sufficiently below the Earth-Moon rotating plane, the illumination condition has a relatively minor impact on m. Therefore, the error of $\hat{\boldsymbol{r}}_{\mathrm{C}}$ is smaller at shorter ranges, and increases with range.

5.4 *Measurement Covariance*

Figure 12 shows the error in range (taken as the difference between the estimated and true range), as well as the error by camera-frame component, against epoch. The images used for this Figure correspond to those from Figure 11. For the error by component,

Table 2: Statistics of measurement error processed through Christian-Robinson algorithm

Fig.	Settings			Mean error, km			Standard deviation, km		
	Anti-alias	Half-pixel comp.	Terrain	x	y	z	x	y	z
10a	False	True	False	0.2744	0.0541	-5.1532	1.0500	1.0364	42.9086
10b	True	True	False	0.3095	-0.1548	30.8501	1.0488	0.8854	38.7992
10c	True	False	False	5.7181	5.2538	30.8498	2.0974	1.9183	38.7992
11	False	True	True	0.3608	0.0687	-7.0976	1.2876	1.3370	54.7969

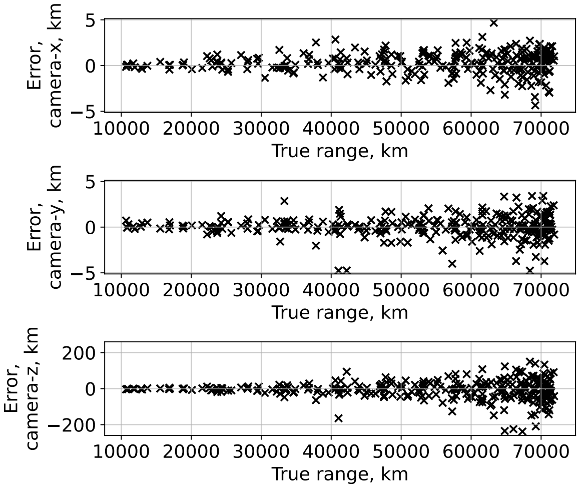

Fig. 11: Effect of terrain on position measurement error in the camera frame, shown against range from the Moon. Images are rendered with terrain, without anti-aliasing, and with half-pixel compensation.

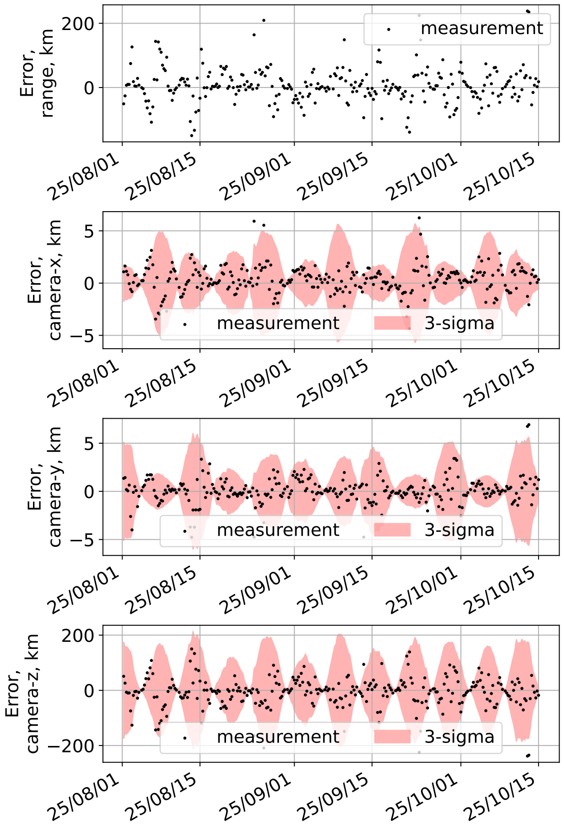

Fig. 12: Position measurement error in range and camera-frame component shown against epoch. The red shaded region corresponds to measurement 3-σ's computed from equation (18).

the red shaded region corresponds to the 3-σ values associated with the measurement, computed by equation (18), which seems to successfully capture the spread of the measurement accurately. The periodic structure in the measurement error as well as the 3-σ of each component is a manifestation of the NRHO's (quasi)-periodic motion, where measurements near perilunes have lower error (and correspondingly lower 3-σ's) while measurements near apolunes are worse.

5.5 *Navigation Filter Performance*

The horizon-based OpNav measurements are incorporated into an EKF to provide state estimates of a spacecraft on the NRHO. An initial filter prior $\mathbf{\Sigma}_{0|0}$ is given by

$$\mathbf{\Sigma}_{0|0} = \text{blockdiag}(\sigma_{r,0}^2 \boldsymbol{I}_{3\times3}, \sigma_{v,0}^2 \boldsymbol{I}_{3\times3}), \tag{36}$$

where $\sigma_{r,0} = 10\,\text{km}$, and $\sigma_{v,0} = 10\,\text{cm/s}$. The diffusion coefficient in the process noise is set to $\sigma_u = 10^{-7}\,\text{m/s}^{3/2}$. The dynamics of the filter are varied compared to the true dynamics of the spacecraft by increasing the SRP ballistic coefficient m/A by 50%; this discrepancy in the dynamics is to be accounted for by the process noise, given by equation

(31). The initial state estimate $\hat{\boldsymbol{\theta}}_{0|0}$ is given by

$$\hat{\boldsymbol{\theta}}_{0|0} \sim \mathcal{N}(\boldsymbol{\theta}(t_0), \boldsymbol{\Sigma}_{0|0}). \tag{37}$$

Figure 13 shows the results of the EKF in terms of state estimate error and standard deviations, in components of the filter's frame. Overall, the filter is able to reduce the initial filter covariance in both position and velocity and shows a consistent performance where the state estimate lies within the filter 3-σ over the vast majority of time. The periodicity of the NRHO motion is visible yet again; this is a combined effect of the periodic nature of the quality of the measurements, as seen in Figure 12, as well as the dynamics itself, where the spacecraft state evolves rapidly around perilune and slowly around apolune.

The spikes observed in the velocity estimates correspond to perilune passes, where the spacecraft rapidly changes its direction of travel as it flies around the Moon. This results in even a small state estimate errors prior to perilune to cause significant error in the velocity component-wise. Nevertheless, this effect is quickly attenuated by measurement updates, as the velocity estimate error quickly reduces immediately after the perilune passes.

Finally, we note that accurate state knowledge near apolune is critical for autonomous stationkeeping, as control maneuvers are commonly executed near apolune, where the dynamics is less sensitive to navigation and maneuvering errors [56, 57]. The filter provides apolune position estimates with errors under ∼5 km and velocity estimates with errors consistently below 2.5 cm/s, which lie between the low (1 km, 1 cm/s) to medium (10 km, 10 cm/s) navigation error magnitudes studied in [56]. The OpNav navigation performance suggests the ability to conduct OpNav-only autonomous GNC on NRHOs.

6. Conclusions

In this work, a high-fidelity simulation environment for horizon-based OpNav has been implemented. The process for choosing the appropriate software, along with the steps involved in configuring the environment, has been discussed. The simulator includes the imaged celestial body including surface features, a directional light source with an angular diameter, and any additional eclipsing body. While this work has focused on using the simulation environment along an NRHO, the same environment could be used for any cislunar orbit without any modification, and for any other horizon-based OpNav applications relative to other celestial bodies by merely swapping the primary body as well as any eclipsing bodies. Images generated through an NRHO have been processed through the Christian-Robinson algorithm and have been incorporated into an EKF, which demonstrated satisfactory navigational performance.

The effect of anti-aliasing as well as flooring/ceiling done by rendering engines on horizon-based OpNav has been studied. Furthermore, in the context of using this framework on an NRHO, the impact of including the lunar terrain, as well as the periodic structure on the illumination, and challenges due to the large variation in range, has been discussed. The latter characteristic of the NRHO poses a challenge for OpNav, the nature of horizon-based OpNav relying on the apparent diameter poses a fundamental degradation of observability along the camera's boresight as the range increases.

Numerical experiments using rendered images are conducted with state-of-the-art methods for identifying the lit limb, which is then converted to position measurements via the SVD-based variant of the Christian-Robinson algorithm. Impacts of rendering effects, the lunar terrain, as well as the large variation in range along NRHOs on the quality of the position measurements, are studied. The imperfection of the obtained measurements highlights the limitation of using analytical models of the lit limbs, with assumptions on things such as zero-mean Gaussian error on identified limb pixels, or on consistent Sun phase angle.

References

[1] K. C. Laurini, B. Hufenbach, J. Hill, and A. Ouellet, "The global exploration roadmap and expanding human/robotic exploration mission collaboration opportunities," in *IAF 66th International Astronautical Congress*, October 2015, pp. 1–9.

[2] B. Hufenbach, K. Laurini, N. Satoh, C. Lange, R. Martinez, J. Hill, M. Landgraf, and A. Bergamasco, "International Missions to Lunar Vicinity and Surface - Near-Term Mission Scenario of the Global Space Exploration Roadmap," in *IAF 66th International Astronautical Congress*, October 2015, pp. 1–11.

[3] "What is CAPSTONE?" https://www.nasa.gov/directorates/spacetech/small_spacecraft/capstone, accessed: September 14, 2023.

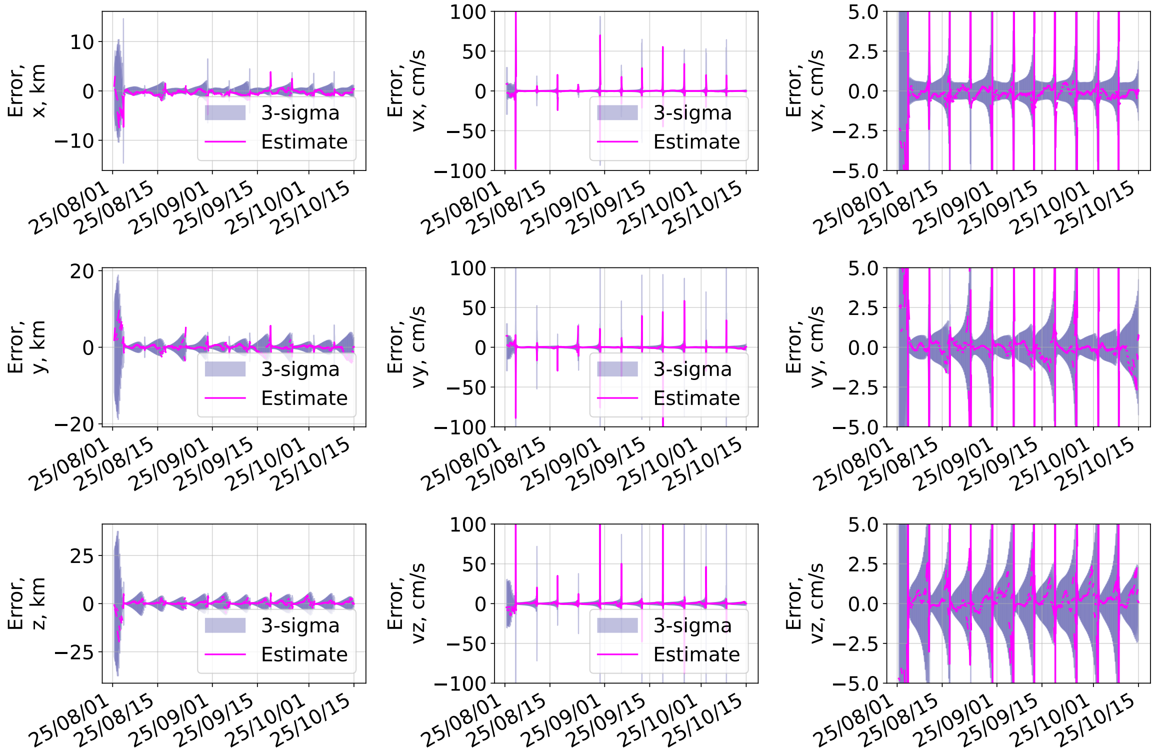

Fig. 13: EKF results using horizon-based OpNav measurements along the NRHO from Figure 11. The position (left column) and velocity (middle/right columns) errors are components in the J2000 frame, which is the frame used within the filter. The right column corresponds to the same data as the middle column, zoomed in.

[4] "Further details on communications issues with NASA's CAPSTONE," https://blogs.nasa.gov/artemis/2022/07/05/further-details-on-communications-issues-with-nasas-capstone/, accessed: September 14, 2023.

[5] "Mission Team Determines Cause of Communications Issues for NASA's CAPSTONE," https://blogs.nasa.gov/artemis/2022/07/07/mission-team-determines-cause-of-communications-issues-for-nasas-capstone/, accessed: September 14, 2023.

[6] J. J. Parker, F. Dovis, B. Anderson, L. Ansalone, B. Ashman, F. H. Bauer, G. D'Amore, C. Facchinetti, S. Fantinato, G. Impresario, *et al.*, "The lunar gnss receiver experiment (lugre)," in *Proceedings of the 2022 International Technical Meeting of The Institute of Navigation*, 2022, pp. 420–437.

[7] N. Babu, "LunaNet Interoperability Specification Document," Tech. Rep., 2022.

[8] Oct 2021. [Online]. Available: https://www.nasa.gov/feature/goddard/2021/lunanet-empowering-artemis-with-communications-and-navigation-interoperability

[9] P. E. Ceruzzi, "Deep space navigation: the apollo viii story," *Quest: The History of Spaceflight Quarterly*, 2010. [Online]. Available: https://repository.si.edu/bitstream/handle/10088/24973/201085SH.pdf

[10] R. H. Battin, *An introduction to the mathematics and methods of astrodynamics.* Aiaa, 1999.

[11] T. Miso, T. Hashimoto, and K. Ninomiya, "Optical guidance for autonomous landing of spacecraft," *IEEE Transactions on Aerospace and Electronic Systems*, vol. 35, no. 2, pp. 459–473, 1999.

[12] J. A. Christian, L. Hong, P. McKee, R. Christensen, and T. P. Crain, "Image-based lunar

terrain relative navigation without a map: Measurements," *Journal of Spacecraft and Rockets*, vol. 58, no. 1, pp. 164–181, 2021. [Online]. Available: https://doi.org/10.2514/1.A34875

[13] S. D'Amico, J.-S. Ardaens, G. Gaias, H. Benninghoff, B. Schlepp, and J. L. Jørgensen, "Noncooperative rendezvous using angles-only optical navigation: System design and flight results," *Journal of Guidance, Control, and Dynamics*, vol. 36, no. 6, pp. 1576–1595, 2013. [Online]. Available: https://doi.org/10.2514/1.59236

[14] "SMART Nav: Giving Spacecraft the Power to Guide Themselves," https://www.jhuapl.edu/interactive/navigating-double-asteroid-redirection-test-on-its-own/, accessed: September 14, 2023.

[15] J. A. Christian, L. Benhacine, J. Hikes, and C. D'Souza, "Geometric Calibration of the Orion Optical Navigation Camera using Star Field Images," *Journal of the Astronautical Sciences*, vol. 63, no. 4, pp. 335–353, dec 2016.

[16] S. Yun, K. Tuggle, R. Zanetti, and C. D'souza, "Sensor configuration trade study for navigation in near rectilinear halo orbits," in *Advances in the Astronautical Sciences*, vol. 171. Univelt Inc., 2020, pp. 2799–2812.

[17] J. A. Christian, "A tutorial on horizon-based optical navigation and attitude determination with space imaging systems," *IEEE Access*, vol. 9, pp. 19 819–19 853, 2021.

[18] "Engineering DOUG Graphics for Exploration (EDGE), JSC Automation, Robotics, and Simulation Division, Houston, Texas," https://software.nasa.gov/software/MSC-24663-1,.

[19] G. N. Holt, C. N. D'Souza, and D. W. Saley, "Orion Optical Navigation Progress Toward Exploration Mission 1," in *2018 Space Flight Mechanics Meeting*, 2018, p. 1978.

[20] P. W. Kenneally, S. Piggott, and H. Schaub, "Basilisk: A flexible, scalable and modular astrodynamics simulation framework," *Journal of Aerospace Information Systems*, vol. 17, no. 9, pp. 496–507, 2020.

[21] T. Teil, H. Schaub, and D. Kubitschek, "Centroid and apparent diameter optical navigation on mars orbit," *Journal of Spacecraft and Rockets*, vol. 58, no. 4, pp. 1107–1119, 2021.

[22] P. Elango, S. Di Cairano, K. Berntorp, and A. Weiss, "Sequential linearization-based station keeping with optical navigation for NRHO," in *AAS/AIAA Astrodynamics Specialist Conference*, 2022.

[23] "Persistence of Vision Raytracer (Version 3.6)," https://www.povray.org/documentation/view/3.6.1/203.

[24] V. Franzese, P. Di Lizia, and F. Topputo, "Autonomous optical navigation for the lunar meteoroid impacts observer," *Journal of Guidance, Control, and Dynamics*, vol. 42, no. 7, pp. 1579–1586, 2019.

[25] C. X. Wu, P. Machuca, L. Felicetti, and J. P. Sanchez, "Autonomous Optical Navigation for Small Spacecraft in Cislunar Space," in *73rd International Astronautical Congress (IAC)*, no. September, 2022, pp. 18–22.

[26] T. Kilduff, P. Machuca, and A. J. Rosengren, "Crater Detection for Cislunar Autonomous Navigation through Convolutional Neural Networks," in *AAS/AIAA Astrodynamics Specialist Conference*, 2023, pp. 1–12.

[27] "Blender - a 3d modelling and rendering package," Blender Foundation, Stichting Blender Foundation, Amsterdam, 2018. [Online]. Available: http://www.blender.org

[28] C. Balossi, "Hardware-in-the-loop validation of a lunar horizon-based autonomous optical navigation strategy," Ph.D. dissertation, Politecnico di Milano, 2022.

[29] G. Napolano, C. Vela, A. Nocerino, R. Opromolla, and M. Grassi, "A multi-sensor optical relative navigation system for small satellite servicing," *Acta Astronautica*, vol. 207, no. March, pp. 167–192, 2023. [Online]. Available: https://doi.org/10.1016/j.actaastro.2023.03.008

[30] C. Buonagura and F. Topputo, "Procedural Minor Body Generator Tool for Data-Driven Optical Navigation Methods," no. May, pp. 1–15, 2022.

[31] K. W. Smith, N. Anastas, A. S. Olguin, M. P. Fritz, R. Sostaric, S. Pedrotty, and T. Tse, "Building Maps for Terrain Relative Navigation Using Blender: An Open-Source Approach," *AIAA Science and Technology Forum and Exposition, AIAA SciTech Forum 2022*, pp. 1–8, 2022.

[32] "Unreal engine 5.1 documentation," Epic Games, 2023. [Online]. Available: https://docs.unrealengine.com/5.1/en-US/,

[33] L. Bingham, J. Kincaid, B. Weno, N. Davis, E. Paddock, and C. Foreman, "Digital Lunar Exploration Sites Unreal Simulation Tool (DUST)," in *2023 IEEE Aerospace Conference*. IEEE, mar 2023, pp. 1–12. [Online]. Available: https://ieeexplore.ieee.org/document/10115607/

[34] T. Phisannupawong, P. Kamsing, P. Tortceka, and S. Yooyen, "Vision-based attitude estimation for spacecraft docking operation through deep learning algorithm," in *2020 22nd International Conference on Advanced Communication Technology (ICACT)*, vol. 2020. IEEE, feb 2020, pp. 280–284. [Online]. Available: https://ieeexplore.ieee.org/document/9061445/

[35] J. Becktor, W. Seto, A. Deole, S. Bandyopadhyay, N. Rahimi, S. Talebi, M. Mesbahi, and A. Rahmani, "Robust Vision-based Multispacecraft Guidance Navigation and Control using CNN-based Pose Estimation," in *2022 IEEE Aerospace Conference (AERO)*, vol. 2022-March. IEEE, mar 2022, pp. 1–10. [Online]. Available: https://ieeexplore.ieee.org/document/9843396/

[36] J. A. Christian and S. B. Robinson, "Noniterative horizon-based optical navigation by cholesky factorization," *Journal of Guidance, Control, and Dynamics*, vol. 39, pp. 2757–2765, 12 2016. [Online]. Available: https://arc.aiaa.org/doi/10.2514/1.G000539

[37] V. Muralidharan, "Stretching directions in cislunar space: Stationkeeping and an application to transfer trajectory design," Ph.D. dissertation, Purdue University, 2021.

[38] D. E. Lee, "Gateway destination orbit model: A continuous 15 year nrho reference trajectory," 2019.

[39] C. H. Acton, "Ancillary data services of nasa's navigation and ancillary information facility," *Planetary and Space Science*, vol. 44, no. 1, pp. 65–70, 1996, planetary data system. [Online]. Available: https://www.sciencedirect.com/science/article/pii/0032063395001077

[40] C. Acton, N. Bachman, B. Semenov, and E. Wright, "A look towards the future in the handling of space science mission geometry," *Planetary and Space Science*, vol. 150, pp. 9–12, 2018, enabling Open and Interoperable Access to Planetary Science and Heliophysics Databases and Tools. [Online]. Available: https://www.sciencedirect.com/science/article/pii/S0032063316303129

[41] "Blender manual 2023 - film," https://docs.blender.org/manual/en/latest/render/cycles/render_settings/film.html#pixel-filter, 2023.

[42] "Blender manual 2023 - smooth shading," https://docs.blender.org/manual/en/latest/scene_layout/object/editing/shading.html, 2023.

[43] E. Wright and N. Petro, "Cgi moon kit," 2019, nASA's Scientific Visualization Studio.

[44] J. A. Christian, "Accurate planetary limb localization for image-based spacecraft navigation," *Journal of Spacecraft and Rockets*, vol. 54, pp. 708–730, 4 2017. [Online]. Available: https://arc.aiaa.org/doi/10.2514/1.A33692

[45] H. Iz, C. Shum, X. Ding, and C. Dai, "Orientation of the Geometrically Best fitting Triaxial Lunar Ellipsoid with Respect to the Mean Earth/Polar Axis Reference Frame," *Journal of Geodetic Science*, vol. 1, no. 1, pp. 52–58, mar 2011.

[46] "Blender manual 2023 - light object," https://docs.blender.org/manual/en/latest/render/lights/light_object.html, 2023.

[47] A. De Ruiter, C. Damaren, and J. Forbes, *Spacecraft Dynamics and Control: An Introduction*. Wiley, 2013. [Online]. Available: https://books.google.com/books?id=8RrKzgEACAAJ

[48] J. A. Christian, "Optical navigation using iterative horizon reprojection," *Journal of Guidance, Control, and Dynamics*, vol. 39, pp. 1092–1103, 5 2016. [Online]. Available: https://arc.aiaa.org/doi/10.2514/1.G001569

[49] R. Hartley and A. Zisserman, *Multiple View Geometry in Computer Vision*, 2nd ed. New York, NY, USA: Cambridge University Press, 2003.

[50] J. A. Christian, "Optical navigation using iterative horizon reprojection," *Journal of*

Guidance, Control, and Dynamics, vol. 39, pp. 1092–1103, 5 2016. [Online]. Available: https://arc.aiaa.org/doi/10.2514/1.G001569

[51] J. Canny, "A computational approach to edge detection," *IEEE Transactions on Pattern Analysis and Machine Intelligence*, vol. PAMI-8, no. 6, pp. 679–698, 1986.

[52] S. Särkkä and L. Svensson, *Bayesian filtering and smoothing.* Cambridge university press, 2023, vol. 17.

[53] J. R. Carpenter and C. N. D'souza, "Navigation Filter Best Practices," Tech. Rep., 2018. [Online]. Available: http://www.sti.nasa.gov

[54] B. Gough, *GNU scientific library reference manual.* Network Theory Ltd., 2009.

[55] B. D. Tapley, B. E. Schutz, and G. H. Born, *Statistical Orbit Determination.* Elsevier Academic Press, 2004.

[56] D. Davis, S. Bhatt, K. Howell, J.-W. Jang, R. Whitley, F. Clark, D. Guzzetti, E. Zimovan, and G. Barton, "Orbit maintenance and navigation of human spacecraft at cislunar near rectilinear halo orbits," in *AAS/AIAA Space Flight Mechanics Meeting*, 2017.

[57] D. Guzzetti, E. M. Zimovan, K. C. Howell, and D. C. Davis, "Stationkeeping analysis for spacecraft in lunar near rectilinear halo orbits," 2017.